Tellus
SERIES A
DYNAMIC
METEOROLOGY
AND OCEANOGRAPHY
PUBLISHED BY THE INTERNATIONAL METEOROLOGICAL INSTITUTE IN STOCKHOLM

Tellus (2009), 61A, 232–249

TELLUS

Urban and ocean ensembles for improved meteorological and dispersion modelling of the coastal zone

By TEDDY HOLT*, JULIE PULLEN and CRAIG H. BISHOP, *Naval Research Laboratory, Monterey, CA*

(Manuscript received 30 April 2008; in final form 10 October 2008)

ABSTRACT

A high-resolution (1.67 km) ensemble transform (ET)-based meso-scale modelling system utilizing urbanization and sea surface temperature (SST) perturbations is used to examine characteristics of sea breeze/heat island interactions and atmospheric transport and dispersion for Tokyo. The ensemble displays a positive spread–skill relationship, with the addition of urban perturbations enabling the ensemble variance to distinguish a larger range of forecast error variances. Two synoptic regimes are simulated. For a pre-frontal period (stronger synoptic flow), there is less variability among ensemble members in the strength of the urban heat island and its interaction with the sea breeze front. During the post-frontal time period, the sea breeze frontal position is very sensitive to the details of the urban representation, with horizontal frontal variation covering the width of the urban centre (∼30 km) and displaying significant impacts on the development and strength of the heat island. Moreover, the dosage values of a tracer released at offshore and urban sites have considerable variability among ensemble members in response to small-scale features such as coastally upwelled water, enhanced anthropogenic heating and variations in building heights. Realistic variations in SST (i.e. warm Tokyo Bay or local upwelling) produce subtle sea breeze variations that dramatically impact tracer distributions.

1. Introduction

Air quality applications have benefitted from ensemble modelling techniques of increasing sophistication (Delle Monache et al., 2006; Zhang et al., 2007). These ensemble approaches build and improve on Monte Carlo specifications (Hanna et al., 2001) and adjoint methods (Menut, 2003) by aiming to provide more dynamic consistency in the structure of the perturbations. Parallel efforts within the dispersion modelling community have applied Monte Carlo analysis to dispersion models (Dabberdt and Miller, 2000) and introduced initial and physics perturbations within an ensemble framework to demonstrate the sensitivity of forecasts to meteorological specification (Warner et al., 2002).

The value of ensemble forecasting in the context of air quality and dispersion modelling has been previously demonstrated in the work cited above. However, numerous questions and gaps remain. For instance, the construction of ensembles described in Delle Monache et al. (2006) does not display a discernible spread–skill relationship. Furthermore, the ensemble studies of Zhang et al. (2007) and Delle Monache et al. (2006) do not account for uncertainties in model representations of the coastal ocean or urban effects, despite emphasizing the coastal urban location of the cities (Houston and Vancouver, respectively). In addition, both papers confine their analysis to 12- and 4-km resolution simulations, thereby neglecting smaller scales. Finally, neither paper explicitly includes data assimilation in their numerical simulations, which limits the predictive skill of the forecasts.

Our work builds on our prior studies of coastal and urban influences on the meteorology of New York City (NYC). We found that the temporal and spatial variability of coastal sea surface temperature (SST) has a pronounced impact on the evolution of the atmospheric planetary boundary layer (PBL; Pullen et al., 2007). In sensitivity studies employing several urban parametrizations, we demonstrated the impact of urban effects on the PBL, as well as the role of small scale features like Kelvin–Helmholtz instabilities in determining contaminant dispersion pathways (Holt and Pullen, 2007; Thompson et al., 2007).

Both the urban morphology and ocean surface temperature distribution strongly influence the fate of tracer distributions in complex coastal urban regions. In our present work, we aim to systematically quantify the relative impacts of SST and urban effects using an ensemble framework incorporating data assimilation and utilizing ∼1-km horizontal resolution. In this paper

*Corresponding author.
e-mail: teddy.holt@nrlmry.navy.mil
DOI: 10.1111/j.1600-0870.2008.00377.x

we describe SST and urban perturbations to an ensemble system configured for the Tokyo metropolitan area (TMA).

In recent decades, Tokyo temperatures have been rising faster than other cities (Ooka, 2007). The average Tokyo urban–rural temperature difference in August is 12 °C, surpassing the urban heat island (UHI) of other Asian mega-cities in magnitude and spatial extent (over 100 km; Tran et al., 2006). The prevalence of sea breeze conditions in the Tokyo region modifies the UHI and can have a mitigating effect on urban temperature extremes. Indeed, the inland displacement and reduced magnitude of the Tokyo UHI in summer relative to winter is attributed to stronger summertime sea breezes (Ichinose et al., 1999).

Studies by Yoshikado and Kondo (1989), Yoshikado (1990) and Ohashi and Kida (2002) have probed in detail the interaction of the sea breeze with the UHI. The sea breeze front typically moves northwest from Tokyo Bay toward Tokyo, a distance of 20 km, over a span of ∼3 h. It has been observed to stall at times at the periphery of urban Tokyo, with associated weak winds located inland of the front. A set of simulations designed to assess the impact of historical land-use changes on sea breeze and UHI dynamics found that the sea breeze front progression was delayed by ∼2 h due to urbanization (Kusaka et al., 2000). In sensitivity simulations, the aforementioned weak wind region scales with the size of the urban area. The model produces a threefold increase in mixing heights as the front subsequently accelerates over the suburbs.

More recent modelling studies incorporating an urban canopy parametrization show skill in reproducing air temperature patterns within Tokyo (Kusaka et al., 2005). In particular, the daytime inland penetration of the sea breeze compared with the nighttime location of highest near-surface air temperatures along the coast is a direct result of the land–sea breeze circulation modifying the UHI.

With advances in urban modelling, much attention has been focused on simulating with greater realism mitigation scenarios to counteract the rapid increase of Tokyo's UHI (Ooka, 2007). For instance, Oda et al. (2007) configured a 1-km resolution semi-urbanized model incorporating observed wintertime SST values in Tokyo Bay. They found no appreciable impact of the SST on air temperatures over Tokyo, due to the predominantly northerly orientation of the winter winds. By contrast, summer conditions are expected to yield rich interactions between the coastal ocean/bay, land topography and the urban morphology and heating—interactions frequently mediated by the evolving sea breeze dynamics.

Our simulations expand the range of parameter space accessible to sensitivity studies by systematically varying key parameters controlling sea breeze and UHI development in the Tokyo metropolitan region. In addition, realistic SSTs are varied within the ensemble framework, and their impact on the UHI is examined. The physical complexity of this coastal urban zone is highlighted in tracer dispersion simulations that encompass processes interacting on multiple space and time scales.

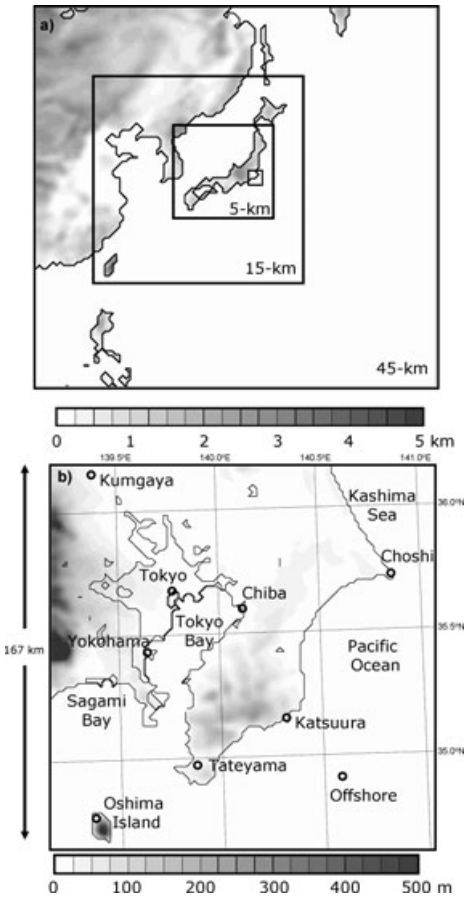

Fig. 1. (a) COAMPS 4-nest model domain for 45-, 15-, 5- and 1.67-km-grid increments with nest 1 terrain shaded, and (b) COAMPS nest 4 (1.67 km) model domain with the eight observation locations used for validation and passive tracer release (see text) in addition to the over-water site (labelled Offshore). Model terrain is shaded and urban areas are indicated by the thin contour.

Section 2 describes the coupled atmospheric and ocean model used in the ensemble system. Section 3 describes the ensemble system methodology, and Section 4 provides a description of the synoptics of a case study. Section 5 discusses results, and Section 6 presents discussion and conclusions.

2. Model description

The atmospheric analysis and forecast models of the Coupled Ocean/Atmosphere Mesoscale Prediction System (COAMPS®;[1] Hodur, 1997; http://www.nrlmry.navy.mil/coamps-web/web/home/) are used for the ensemble simulations. The COAMPS configuration over the TMA has four 2-way interactive nests of grid increments 45-, 15-, 5- and 1.67-km with 116 × 110, 172 × 184, 241 × 271 and 100 × 100 gridpoints for the four nests, respectively (Fig. 1). The emphasis is on

[1]COAMPS is a registered trademark of the Naval Research Laboratory.

the highest resolution 1.67-km grid; so, subsequent figures and discussion, with the exception of the synoptic discussion, will pertain to grid 4. There are 40 vertical sigma-z levels from 10 to 29 385 m with increased vertical resolution in the lower levels. There are 11 levels below 900 m, with the lowest four levels at 10, 30, 55 and 90 m above ground level (agl).

The COAMPS uses a finite-difference approximation to the fully compressible, non-hydrostatic equations with a terrain-following vertical coordinate transformation, and second-order, accurate, finite difference schemes in time and space. A time splitting technique with a semi-implicit formulation for the vertical acoustic modes is used to efficiently integrate the compressible equations (Klemp and Wilhelmson, 1978). The COAMPS physics used for the PBL and subgrid-scale turbulence processes are represented by a turbulent kinetic energy (TKE) scheme following Mellor and Yamada (1982), with the surface layer parametrized after Louis et al. (1982). The four-layer COAMPS land–surface-hydrology model is the Weather Research and Forecasting (WRF) of National Centers for Environmental Prediction, Oregon State University, Air Force, Office of Hydrology (NOAH) model (Holt et al., 2006) and, for this study, is initialized from 00 UTC 25 June 2005 Air Force Weather Agency (AFWA) Agricultural Meteorological Model (AGRMET) analysis soil temperature, moisture and water profiles at 10-, 40-, 100- and 200-cm soil depth. Urban effects are parametrized using the roughness approach or with an urban canopy parametrization (described in section 3). The radiation scheme is that of Harshvardhan et al. (1987). Moist processes on the 45- and 15-km grids are simulated using a modified Kain and Fritsch (1993) cumulus parametrization but are treated explicitly on grids 3 and 4 with a modified Rutledge and Hobbs (1983) and Khairoutdinov and Kogan (2000) moist physics parametrization.

The COAMPS atmospheric forecast model is run in concert with a data assimilation scheme. Multivariate optimal interpolation (MVOI; Barker, 1992) analyses of upper-air soundings, surface, aircraft and satellite observations are quality controlled and blended with the previous COAMPS forecast fields, using an incremental update data assimilation procedure (Hodur, 1997).

To better assess the effect of the ocean on COAMPS atmospheric ensemble forecasts, SSTs are handled in two different ways. The first is to use in stand-alone mode (i.e. not coupled to an ocean forecast model) the operational Navy Coupled Ocean Data Assimilation (NCODA) system to provide SST fields from an MVOI analysis of satellite and in situ observations (Cummings, 2006). For this method the SST is held fixed over the atmospheric forecast time period. The second method is to use the ocean model within the coupled system (Navy Coastal Ocean Model, NCOM; Martin, 2000). The ocean model is not currently operational in the COAMPS ensemble framework. Therefore, the COAMPS atmospheric forecast model was run uncoupled for June 2005 at 45- and 15-km resolution, with 15-km forcing saved every hour to drive the ocean model in an off-line manner. The NCOM, using the NCODA data assimilation system (hereafter termed NCOM/NCODA), was then run doubly-nested for the COAMPS 5- and 1.67-km grids, using the COAMPS 15-km forcing with a 12-h ocean data assimilation update cycle (at 00 UTC and 12 UTC), creating forecasts out to 12 h. The outer NCOM/NCODA 5-km grid used global Hybrid Coordinate Ocean Model (HYCOM)/NCODA initial and boundary conditions (Chassignet et al., 2007). The NCOM/NCODA analysis and hourly forecast fields of SST on the 1.67-km grid were then supplied to the COAMPS atmospheric forecasts from 06 UTC 25 June to 18 UTC 30 June 2005. Thus for this method, the SST is variable over the atmospheric forecast time period.

3. Ensemble system

3.1. Description

The basis of the COAMPS ensemble system is a computationally inexpensive ensemble transform (ET) method used for generating high-resolution initial perturbations for regional ensemble forecasts (Bishop and Toth, 1999; Bishop et al., 2008). The method provides initial perturbations that (1) have an initial variance consistent with the best available estimates of initial condition error variance, (2) are dynamically conditioned by a process similar to that used in the breeding technique, (3) sum to zero at the initial time, (4) are quasi-orthogonal and equally likely and (5) respect meso-scale balance constraints by ensuring that each initial perturbation is a linear sum of forecast perturbations from the preceding forecast. Because each ET analysis perturbation is a distinct sum of forecast perturbations, each analysis perturbation contains all of the scales resolved by the forecast model and is well suited to variable resolution models.

One member of the ensemble is designated as the control (hereafter mbr000) and is initialized with the minimum error variance state estimate obtained from a data assimilation scheme. The MVOI cycling with COAMPS does not produce an estimate of the error variance of its analyses. However, the MVOI background error covariance model is similar to that of Navy's Variational Data Assimilation System (NAVDAS) in that (1) their correlation length scales are the same order of magnitude, (2) they both use isotropic correlation functions and (3) they both incorporate geostrophic balance. These similarities motivate us to use the NAVDAS estimate of analysis error variance for the global model interpolated onto the COAMPS grid, as our estimate of analysis error variance (Bishop et al., 2008). This is an intermediate procedure, as later versions of the COAMPS ensemble system will use NAVDAS as its data assimilation scheme. The remaining ensemble members are initialized with perturbed initial conditions derived from the ET technique.

3.2. Methodology

Three sets of experiments are conducted to examine SST and urban effects in the ensemble system (see Table 1). All experiments use the ET method as described above, with different

Table 1. Description of the three COAMPS ensemble experiments

Exp. name	Members	SST	Urban perturbations
Exp-1	Control + 10	Fixed (NCODA)	No
Exp-2	Control + 10	Fixed (NCODA)	Yes
Exp-3	Control + 20	Time variable (NCOM/NCODA)	Yes

permutations of SST and/or urban perturbations. The first experiment (EXP-1) uses analysed SSTs from NCODA (held fixed over the length of the forecast) and no urban perturbations to isolate the effects of the ET method and serves as a baseline against which the other experiments may be compared. The second experiment (EXP-2) is the same as EXP-1 but includes urban perturbations (as described below). The third experiment (EXP-3) uses time varying SSTs from NCOM/NCODA and urban perturbations (resulting in twice as many ensemble members).

For each of the experiments, a series of simulations is conducted every 6 h for 6 d (25–30 June 2005) for the control and 10 (or 20) ensemble members. The first simulation starting at 00 UTC 25 June 2005 uses initial fields from the 1-degree Navy Operational Global Atmospheric Prediction System (NOGAPS) T119L30 ET ensemble, interpolated to the COAMPS domain (McLay et al., 2007). In addition, the lateral boundary conditions for COAMPS grid 1 are also obtained from the different global ET states, and the COAMPS physics are uniquely perturbed for each member (as shown in Table 2 and discussed in detail below).

The control COAMPS simulation is derived from the global NAVDAS analysis while the other ensemble states correspond to perturbed global states. For subsequent COAMPS forecasts, the procedure for creating ET initial perturbations is applied using the previous 6-h forecasts as described in Bishop et al. (2008) and summarized here: (1) compute the mean and perturbations of the 6-h ensemble forecast; (2) retrieve the MVOI analysis and the estimate of its error variance from NAVDAS; (3) create analysis perturbations from the transformation matrix; (4) add the analysis perturbations to the analysis to create an ensemble of analyses and (v) use these to initialize and run the next ensemble of forecasts. Throughout the experiments, mbr000 is always the unperturbed or control forecast. From 00 UTC 25 June to 18 UTC 30 June 2005, the 6-h analysis-forecast cycle is repeated. At 00 and 12 UTC, 12-h ensemble forecasts are performed (but at 06 and 18 UTC only 6-h forecasts are performed, purely for

Table 2. Description of urban and SST parameters used in the ensemble system. The bold values indicate values different from the default. All members use the NOAH Land Surface Model (LSM) and AGRMET initialization, and the control member uses only the roughness approach for urban effects

Member	Urban	h_{urb} (m)	f_{urb}	f_{roof}	q_{urb} (Wm^{-2})	k_{ext}	U_{class}*	SVF	SST
0 (Control)	No*								Anal
1 (LANL defaults)	LANL	12	0.6	0.35	20	0.1			mbr011 -1 d
2 (WRF defaults)	WRF	7.5	0.6		0		HIR	0.57	mbr012 -2 d
3 (LANL urban fract)	LANL	12	**0.1**	**0.05**	20	0.1			mbr013 -3 d
4 (LANL build hts)	LANL	**100**	0.6	0.35	20	0.1			mbr014 -4 d
5 (LANL anthro heat)	LANL	12	0.6	0.35	**100**	0.1			mbr015 -5 d
6 (LANL rad extinct)	LANL	12	0.6	0.35	20	**0.3**			mbr016 -6 d
7 (WRF urban fract)	WRF	7.5	**0.1**		0		HIR	0.57	mbr017 -7 d
8 (WRF urban class)	WRF	7.5	0.6		0		**COM**	0.48	mbr018 -8 d
9 (WRF urban class)	WRF	5	0.6		0		**LIR**	0.62	mbr019 -9 d
10 (WRF sky view fact)	WRF	7.5	0.6		0		HIR	**0.10**	mbr020 -10 d

Note: Urban parameters are building height (h_{urb}), urban fraction (f_{urb}), roof fraction (f_{roof}), anthropogenic heating (q_{urb}), radiation extinction coefficient (k_{ext}), urban classification (U_{class}) and sky view factor (SVF), and the values shown are applied to all urban gridpoints. U_{class} is either commercial (COM), high intensity residential (HIR) or low intensity residential (LIR). The seven parameters for each classification are indicated within the brackets as: building height (h_{urb}), momentum roughness length (z_{0m}), heat roughness length (z_{0h}), zero plane displacement height (z_{0d}), normalized building height (h_{norm}), building volumetric parameter ($build_{volp}$) and sky view factor (SVF). The SST is from the NCODA or NCODA/NCOM analysis for the control and is time-lagged for members 011 to 020.

$U_{class} = f(h_{urb}; z_{0m}; z_{0h}; z_{0d}; h_{norm}; build_{volp}; SVF)$;

HIR = (7.5 m; 0.75 m; 0.75 m; 1.5 m; 0.42; 0.4; 0.57);

COM = (7.5 m; 1.0 m; 1.0 m; 2.0 m; 0.56; 0.5; 0.48);

LIR = (5.0 m; 0.5 m; 0.5 m; 1.0 m; 0.35; 0.3; 0.62).

*roughness approach.

computational expediency). Thus, the 6-d experiment provides 23 6-h ET and 11 12-h ensemble forecasts (excluding the initial 00 UTC 25 June cold start).

3.3. *Physics perturbations*

To account for model uncertainty in representations of physical processes, differing but physically realizable values of SST and urban parameters are used. Table 2 shows the unique combination of SST and urban perturbations used on grid 4. For SST, EXP-1 and EXP-2 use NCODA analyses generated every 6-h data assimilation cycle that are kept constant over the forecast time period. For EXP-3, the NCOM/NCODA SST analysis and hourly forecasts are used, with the perturbations time-lagged from 1 to 10 d (i.e. mbr011 uses the NCOM/NCODA 1.67-km SST fields from 1 d earlier, mbr012 uses fields 2 d earlier, etc., with mbr020 using fields 10 d earlier). Time-lagging is chosen because it is a simple perturbation method, yet one that provides reasonable ensemble spread.

Hourly high-resolution model-derived SSTs encapsulate coastal ocean processes like local upwelling and advective events that may not appear in analyses of observed data, especially when the model domain is quite small (Pullen et al., 2007). The SST spatial variability is illustrated in Fig. 2, showing the 1.67-km control SST valid at 00 UTC 30 June, obtained from the NCOM/NCODA analysis and the 1-d lag (mbr011) and 10-d lag (mbr020) differences from the control. In the control, the northern portion of Tokyo Bay is warmer due to the shallow bathymetry and dominance of short-wave surface heating. Temperatures in Tokyo Bay are not modified significantly in the ensemble members. By contrast, a warm SST pool in Sagami Bay is encircled by cooler waters from the south, forming a cyclonic circulation cell in the control member that is altered in magnitude and location in the ensemble members. As well, SST striations south of Choshi in the control member are replaced by local upwelling processes occurring at different times in the ensemble members.

For the urban perturbations, two different urban canopy models embedded within COAMPS are used: the WRF Urban

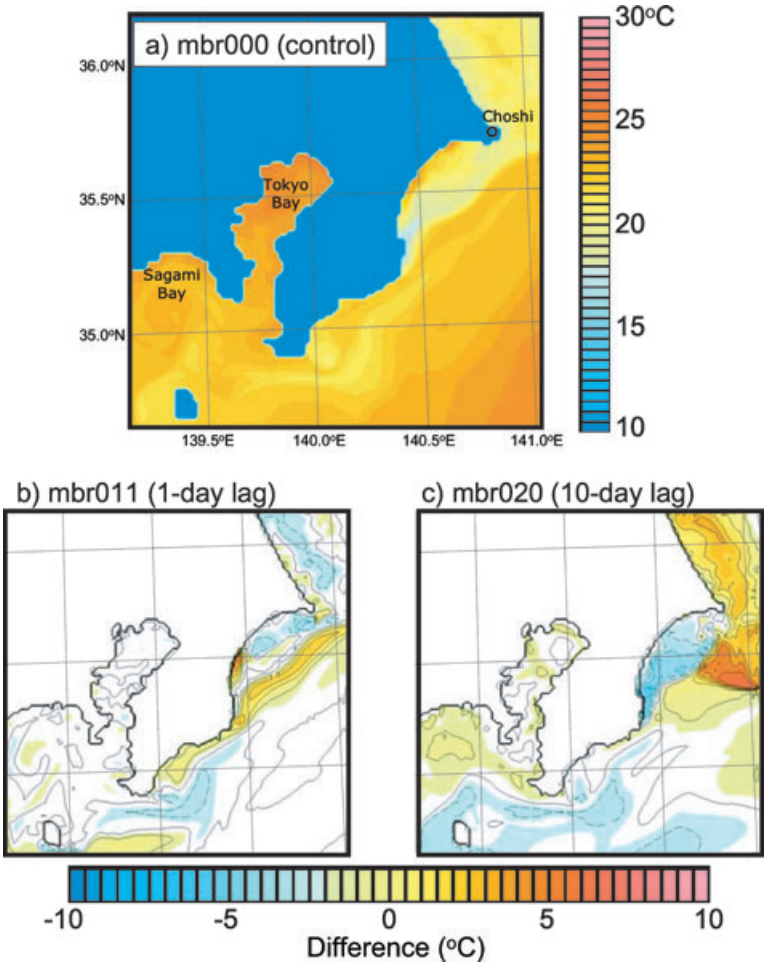

Fig. 2. (a) COAMPS nest-4 (1.67 km) control sea surface temperature (SST) analysis valid at 00 UTC 30 June 2005 from NCOM/NCODA, and SST difference (control-mbr) for (b) mbr011 (1-d time lag) and (c) mbr020 (10-d lag). The contours are every degree and dashed for negative values.

Canopy Model (hereafter WRF-UCM; Kusaka et al., 2001; Holt and Pullen, 2007) and the Los Alamos National Laboratory (hereafter LANL; Brown and Williams, 1998) urban model. These two models both represent basic urban dynamical and thermodynamical processes, such as building drag, turbulence and wake generation and radiation/heating effects through sophisticated parametrizations. However, the LANL urban model uses a vertical multilayer approach to parametrize the urban effects, whereas the WRF-UCM is a single-layer model.

Numerical sensitivity results from Holt and Pullen (2007) for the NYC metropolitan area, using these two urban models show that the differing treatment of urban processes can have a significant impact on urban canopy layer temperatures, moisture and winds. For example, WRF-UCM parametrizes wall and road effects and typically maintains the UHI more realistically through increased nocturnal warming from wall/road surfaces. The ground heat flux for WRF-UCM is usually much larger during the daytime than for LANL, effectively shifting the period of positive sensible flux later, into the early evening. This helps to maintain the near-surface mixed layer at night in WRF-UCM and sustains the nocturnal UHI. Alternatively, the multilayer LANL winds show more dependence on urbanization than WRF-UCM. The decrease in urban canopy wind speed is most prominent for LANL during both day and nighttime over heavily urbanized areas, with the daytime decrease generally over the region of tallest building heights whereas the nighttime decrease is influenced by both building height as well as urban fraction.

The parameters perturbed in the two urban models are those that provide the most variability (or sensitivity), based on the authors' experience with COAMPS simulations using WRF-UCM and LANL. For example, a first order effect impacting basic dynamic and thermodynamic urban processes within urban canopy models is the height over which the parametrization is applied, that is, the height of the urban canopy (h_{urb}). Because the WRF-UCM is a single layer model, this height is always the lowest level of the model (here 10 m). However, LANL can use multiple levels to define h_{urb}, and thus is varied (to values as large as 10 times the default). Another parameter of interest is the amount of anthropogenic heating within h_{urb}. Research has shown that this heating can vary by more than 120% over the TMA (Saitoh et al., 1996). The WRF and LANL default values used here range from 0 to 20 W m^{-2} and are perturbed to a maximum value of 100 W m^{-2} (to approximate the TMA anthropogenic heating, which can be as large as 400 W m^{-2} for summer daytime at localized areas; Ichinose et al., 1999). The other perturbed urban parameters are urban classification (designated as commercial, high-intensity residential, or low-intensity residential), urban fraction (fraction of grid cell that is classified as urban), roof fraction (fraction of grid cell that is covered by roof), sky view factor (relationship between the visible area of the sky and the portion of the sky obscured by buildings, viewed from a specific observation point) and radiation extinction (weighting function expressing fraction of net radiation reaching the surface). These parameters are similarly perturbed to values within ranges given in the literature (see Table 2). In contrast to the two urban models described above, the control member uses only the roughness approach to parametrize urban effects by increasing the albedo, surface roughness and soil conductivity over urban regions. Thus, the control member includes a baseline urban representation incorporating first-order effects that is the approach commonly used by operational NWP models to account for urban impacts on weather.

4. Synoptic description

We choose a time period containing a frontal passage and multiple sea breeze events to investigate the impact of SST and urban perturbations on the ensemble system. The synoptic conditions during the 6-d period are characterized by two distinctly different low-level flow patterns. During the initial 3 d (25–27 June 2005) high surface pressure and weak upper-level forcing occur over the western North Pacific Ocean to the southeast of Asia, as shown in the 00 UTC 27 June global analysis (Fig. 3). Over the model domain (in the vicinity of the TMA), a generally steady south-southwesterly low-level flow persists along with a

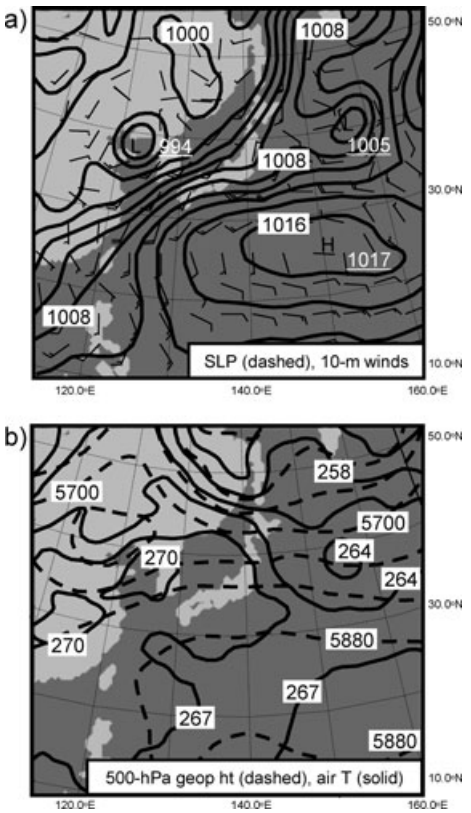

Fig. 3. NOGAPS analysis valid at 00 UTC 27 June 2005 over the COAMPS nest-1 domain of (a) sea level pressure (hPa; dashed) and 10-m winds (barbs) and (b) 500-hPa geopotential height (m; dashed) and air temperature (K; contours).

retardation of the local sea-breeze circulation, a strong diurnal cycle, minimal cloudiness and no precipitation. These conditions are pervasive until approximately 00 UTC 28 June. The synoptic pattern shifts after 28 June with the passage of several upper-level troughs to the north. Over Japan this results in moister, cooler low-level flow for the latter 3 d of the study (28–30 June) and more overcast conditions (including some precipitation), particularly over southern Japan. Winds are generally weaker, but with more pronounced sea breezes.

5. Results

5.1. Ensemble performance

Our metrics for ensemble performance are based on the following goals: (1) to achieve initial condition perturbations whose scale is concordant with the high resolution inner nests; (2) to obtain an ensemble variance that is a useful predictor of forecast error variance; (3) to realize a weighted ensemble mean that minimizes forecast error variance and (4) to improve our understanding of model physics through a comparison of individual member performance.

To address (1), Fig. 4 shows the initial state (00 UTC 28 June) of one member's (mbr001) 10-m potential temperature (θ) perturbations from grid 1 and grid 4. The grid 1 perturbations are shown only over the grid 4 domain for direct comparison. The

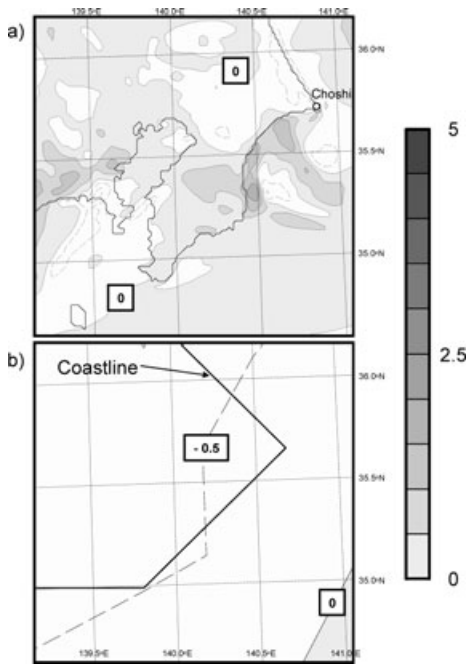

Fig. 4. COAMPS analysis perturbations for EXP-3 mbr001 valid at 00 UTC 28 June 2005 for 10-m potential temperature (°C) for (a) nest-4 (1.67 km), and (b) nest-1 (45 km) shown on the nest-4 domain. Positive values are shaded, negative values are dashed and the contour interval is 0.5 °C.

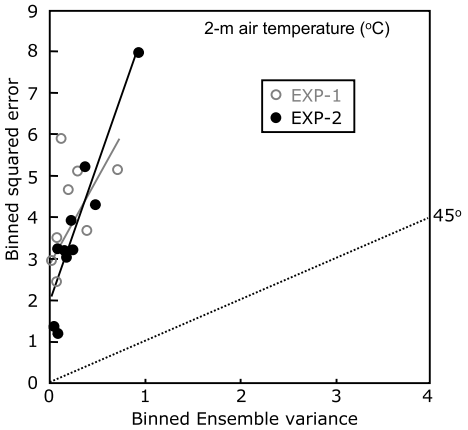

Fig. 5. Spread-skill plot of COAMPS EXP-1 and EXP-2 ensembles for nest-4 (1.67 km) 6-h forecasts from 06 UTC 25 June to 00 UTC 1 July 2005 of 2-m air temperature (°C).

structure of the perturbations on the 1.67-km grid, in contrast to the 45-km grid, demonstrates that the analysis perturbation contains all of the scales resolved by the forecast model, as was anticipated in Section 3.1. The high-resolution perturbations are reflective of the environment as shown by the occurrence of the perturbed warmer air values located in the vicinity of the higher control SSTs southwest of Choshi (Fig. 4a).

The spread–skill relationship is used to evaluate the ability of the ensemble variance to predict forecast error variance (2, above; Fig. 5). Squared differences between verifying observations and the control forecasts are paired with the variance of the ensemble forecasts to create the spread–skill plot. These data pairs are then ordered from smallest ensemble variance to largest ensemble variance. The ordered pairs are then placed into approximately equally populated bins of pairs having similar ensemble variances. Within each bin the mean value of the squared differences between forecasts and observations is computed, as is the bin average of ensemble variance. Figure 5 shows the bin-averaged squared difference of forecasts and observations of 2-m air temperature for EXP-1 (where no model perturbations were used) and EXP-2 (urban perturbations) as a function of bin averaged ensemble variance. It indicates that forecast error variance is a monotonically increasing function of our ensemble variance and hence that our ensemble successfully distinguishes large error variance from small error variance. Furthermore, the addition of urban perturbations (EXP-2) enables the ensemble variance to distinguish a larger range of forecast error variances. The EXP-3 spread–skill relationship (not shown) is similar to EXP-2.

Development of a weighted ensemble mean that minimizes forecast error variance is planned, but as a first step to satisfy (3), the EXP-3 bias and standard deviation (σ) of the ensemble mean of 2-m air temperature and 10-m wind speed are both shown to be smaller than that of the control (Fig. 6). EXP-3 provides ensemble information about both urban and SST

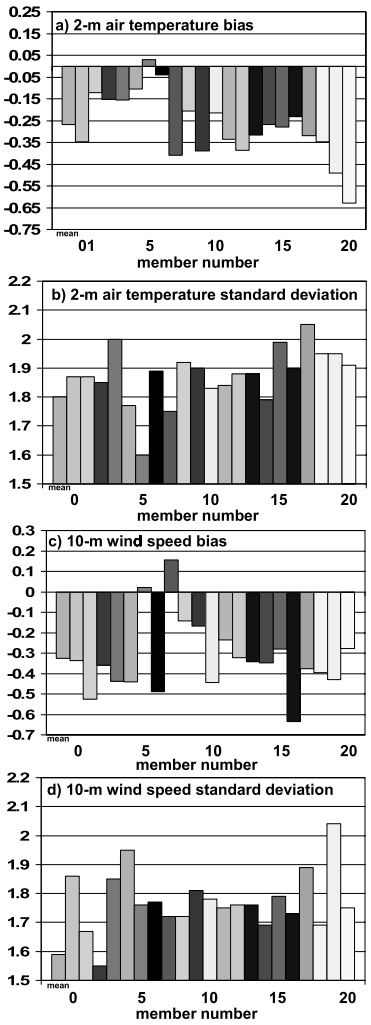

Fig. 6. COAMPS nest 4 (1.67 km) statistics for EXP-3, including the ensemble mean, for 12-h forecasts from 12 UTC 25 June to 12 UTC 30 June 2005 of (a) 2-m air temperature bias (°C), (b) 2-m air temperature standard deviation, (c) 10-m wind speed (m s^{-1}) bias and (d) 10-m wind speed standard deviation validated using the eight sites given in Fig. 1b.

perturbations (unlike EXP-1 and EXP-2); so, it will be the focus of the remainder of the study.

As a means to realizing (4), member statistics are compared to assess which perturbations have the most positive (or negative) impact. Comparing ensemble members that use NCODA (non time-lagged) SSTs (members 001 to 010) with members with NCOM/NCODA (time-lagged) SSTs (members 011 to 020) illustrates the SST impact for a given urban perturbation. Generally, there are larger differences for 2-m air temperature than for 10-m winds, in accordance with the expected influence of SST perturbations. Specifically, members 001 to 010 have smaller temperature bias and σ (average = –0.18 and 1.84 °C, respectively) compared with members 011 to 020 (average = –0.36 and 1.91 °C), whereas members 001 to 010 have smaller wind speed bias and σ (average = –0.28 and 1.76 m s^{-1}) compared with members 011 to 020 (average = –0.36 and 1.79 m s^{-1}).

The statistics allow us to further differentiate among individual members. Among SST perturbation members (011 to 020), the longer time-lagged members are generally the least skillful, indicating the importance of contemporaneous SSTs. For urban perturbation members (001 to 010), member 005, in which anthropogenic heating is increased to 100 W m^{-2} for urban areas, is the most skillful for 2-m air temperature (mean bias = 0.03 °C; σ = 1.60 °C). This clearly indicates that the default anthropogenic heating (∼0–20 W m^{-2}) is too small for Tokyo and emphasizes the importance of anthropogenic heating in sustaining the higher urban canopy temperatures for the TMA. A larger value (i.e. 100–200 W m^{-2}) could have been chosen, but one of the goals of this study is to use the default parameters of the urban models. For wind speed, there is more uniformity among both urban and SST members, with an average wind bias = –0.32 m s^{-1} and σ = 1.77 m s^{-1}. This indicates that the wind speed is not particularly sensitive to the urban parameters, at least for this time period and area. Members 005 and 007 are the only members with a positive wind bias, and member 002 has significantly smaller σ than all other members. For member 005 there is positive feedback from the enhancement in urban canopy warming from anthropogenic heating, resulting in increased urban canopy wind speeds. Members 002 and 007 use the WRF urban canopy model with mbr007 having a significantly smaller urban footprint (0.1 urban fraction versus 0.6), resulting in decreased urban drag and larger mean wind speeds. This indicates that the urban fraction default value (0.6) is too large because the winds on average are too weak in the majority of members using that value.

5.2. *Daytime case study (Pre- versus post-frontal)*

Observations at Tokyo and COAMPS EXP-3 low-level forecasts of the control member, ensemble mean and σ over the 6-d period are shown in Fig. 7. The pre- and post-frontal periods discussed in Section 4 are clearly evident in the sea level pressure (SLP) time-series, with the frontal passage (minimum SLP = 999 hPa) occurring at approximately 18 UTC 27 June (Fig. 7a). For the pre-frontal period (25–27 June), COAMPS forecasts (including the control member and ensemble mean) generally underestimate maximum and minimum temperatures (Fig. 7b) and dew point depression (Fig. 7c), resulting in a generally cooler and moister PBL than observed. Wind speed and direction are generally well forecast for the pre-frontal period (Figs. 7d and e). The ensemble mean is generally a better predictor of SLP, temperature, moisture and winds than the control forecast (in agreement with Fig. 6). The ensemble spread shows no systematic differences from the beginning to the end of the time period (with a two standard deviation range of approximately 0.4–1.0 hPa for SLP, 0.3–0.8 °C for air temperature, 0.6–2.1 °C for dew point

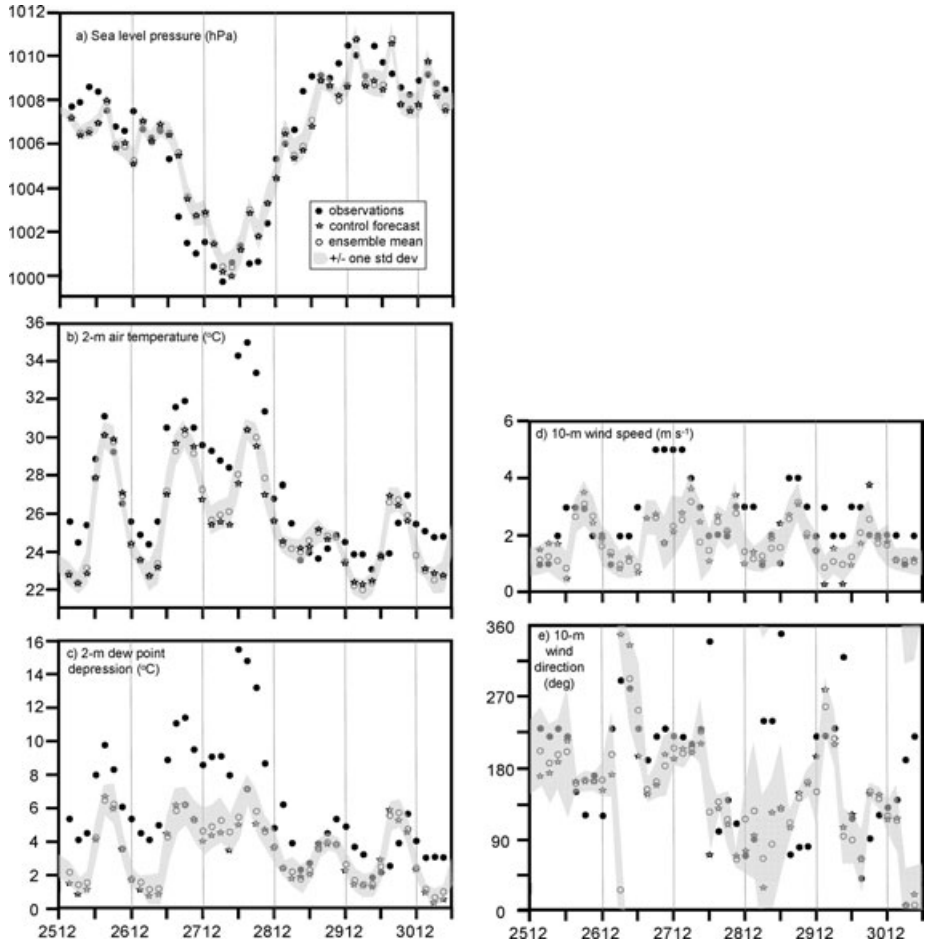

Fig. 7. Time series at Tokyo from 12 UTC 25 June (labelled 2512) to 00 UTC 1 July 2005 of observations (solid circles) and COAMPS nest 4 EXP-3 control forecast (stars) and ensemble mean (open circles) for 3-, 6-, 9- and 12-h forecasts concatenated together and ± one standard deviation about the mean shaded for (a) sea level pressure (hPa), (b) 2-m air temperature (°C), (c) 2-m dew point depression (°C), (d) 10-m wind speed (m s^{-1}) and (e) 10-m wind direction (deg). The frontal passage is at 18 UTC 27 June.

temperature and 0.8–2.0 m s^{-1} and 40°–170° for wind speed and direction). However, the characteristics of the COAMPS post-frontal forecasts are significantly different from the pre-frontal forecasts—with COAMPS temperatures and winds capturing the diurnal evolution much better. Because of these differences, two daytime 12-h periods, one pre-frontal (00–12 UTC 27 June) and one post-frontal (00–12 UTC 30 June) will be compared.

Figure 8 shows the COAMPS control 6-h forecast valid 06 UTC 27 June, illustrating the pre-frontal near-surface conditions. The 10-m winds are uniform from the south-southwest over Tokyo Bay and the Pacific Ocean south of Choshi (Fig. 8a), in agreement with observations (Fig. 8b). The cooler, moister air over Tokyo Bay is clearly advected north-northwest between Tokyo and Chiba, reaching approximately 40–50 km inland. The strong low-level flow generally overwhelms the local sea breeze flow, with the exception of inland of the Kashima Sea and just south of Choshi, where the sea breeze front is delineated by the maximum in PBL vertical velocity located approximately 10–20 km inland (Fig. 8b). Because of the stronger synoptic forcing, there is much less variability among ensemble members in the strength of the UHI and its interaction with the sea breeze front as compared to the post-frontal conditions.

The post-frontal COAMPS 6-h forecast valid 06 UTC 30 June shows clear evidence of multiple sea breeze fronts over the TMA (Fig. 9). The sea breeze front over the Tokyo urban region is illustrated by the heavy solid line, with other prominent fronts located inland from Choshi, as well as along the northern shore of Sagami Bay into the mouth of Tokyo Bay (Fig. 9a). For the sea breeze front over Tokyo, the quadrilateral box indicates the spatial extent of the location of the front for all 20 ensemble members and is used to represents the positional range of the front. The extent of the box from Tokyo Bay to the north-northwest (oriented along the propagation direction of sea breeze front) covers approximately the core urban Tokyo area—a distance of ∼30 km. The location of the front is determined subjectively based on horizontal temperature, dew point

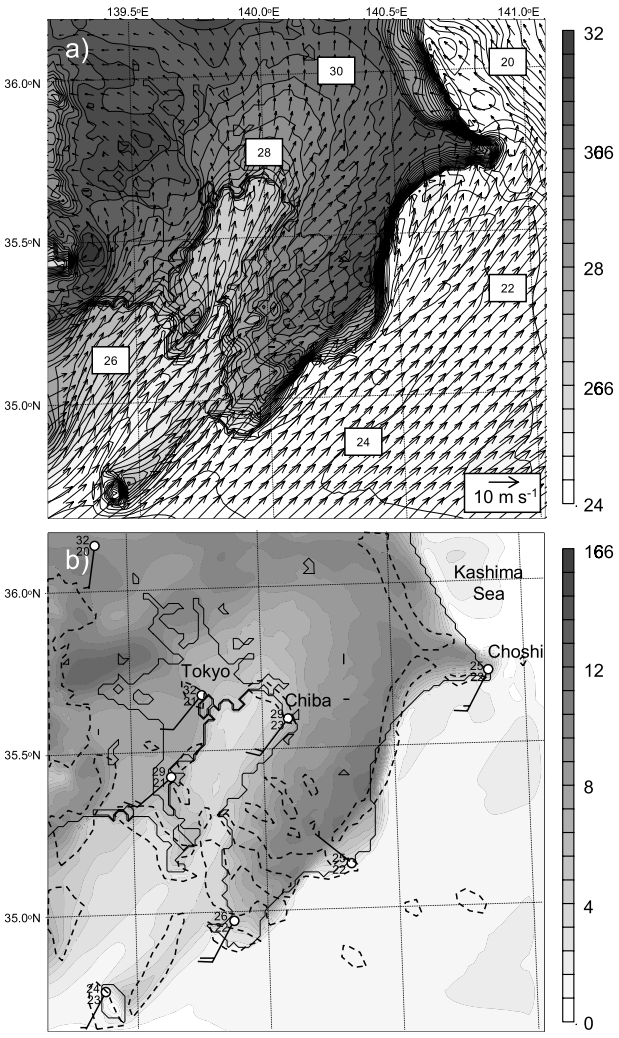

Fig. 8. COAMPS grid 4 (1.67 km) EXP-3 control member 6-h forecast valid 06 UTC 27 June of (a) 10-m winds (shown every third gridpoint) and air temperature (shaded with contour interval = 0.4 °C) and (b) 10-m dew point depression (shaded, interval = 0.4 °C), 210-m vertical velocity greater than 5 cm s^{-1} (dashed contour) and station observations (air and dew point temperature, °C, and winds, full barb = 5 m s^{-1}).

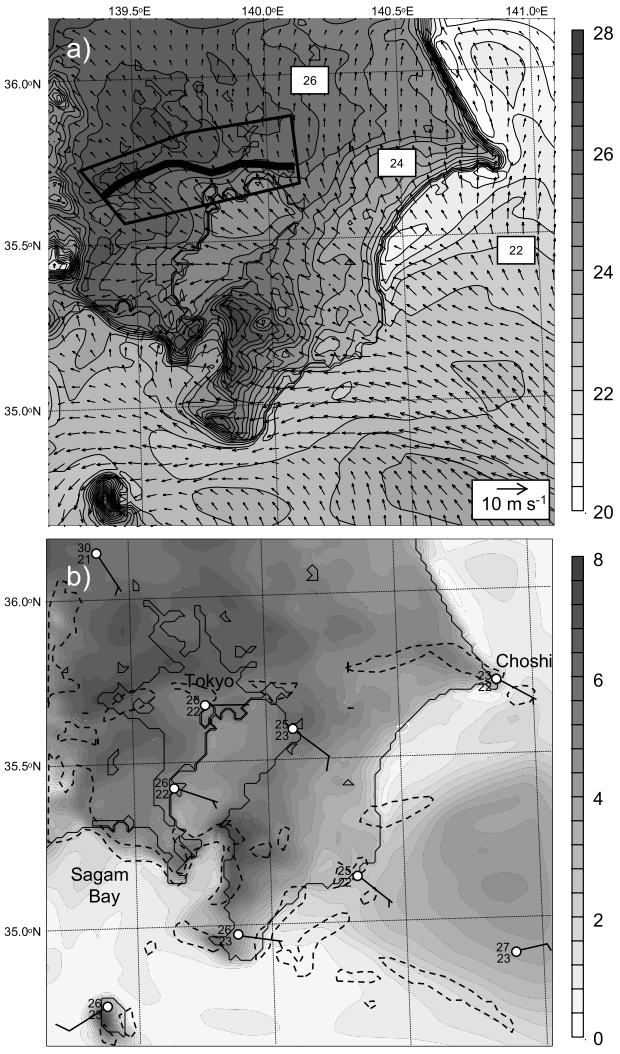

Fig. 9. COAMPS grid 4 (1.67-km) EXP-3 control member 6-h forecast similar to Fig. 8 but valid 06 UTC 30 June. The subjective location of the sea breeze front over Tokyo is shown with a heavy solid line, and the ensemble spread of the location of the sea breeze front is indicated in (a) by the quadrilateral box.

depression and wind direction gradients, as well as PBL vertical velocity. Figure 9b shows the 10-m dew point depression and 210-m agl vertical velocity greater than 5 cm s^{-1}. The significant sea breeze fronts are clearly indicated over the three regions mentioned above. The cooler, moister inflow into Tokyo is also prominently shown in the low-level temperature and dew point depression and serves to mitigate the effects of the UHI. The Tokyo observation shows weaker winds from the east, suggesting that the front has not yet reached the urban area, unlike the control member forecast.

In comparison to the control, ensemble member 004 (with enhanced building heights) shows the largest differences in location, extent and strength of the sea breeze front over Tokyo (Fig. 10). The winds are uniformly weaker over Tokyo, the temperatures higher (but with a significant downwind UHI maximum to the northwest; Fig. 10a) and no signature of vertical velocity maximum (Fig. 10b). The front pushes further inland of the Sagami Bay (compared with Fig. 9a), but is blocked by the urban region to the east and the higher terrain to the west and is funnelled west of Tokyo, as the region of largest vertical velocity is aligned southeast-northwest of Tokyo (Fig. 10b). Thus, the sea breeze front skirts around the urban area marked by larger buildings in contrast to the control.

Among the perturbed SST members, the largest differences compared with the control occur over the near-shore waters

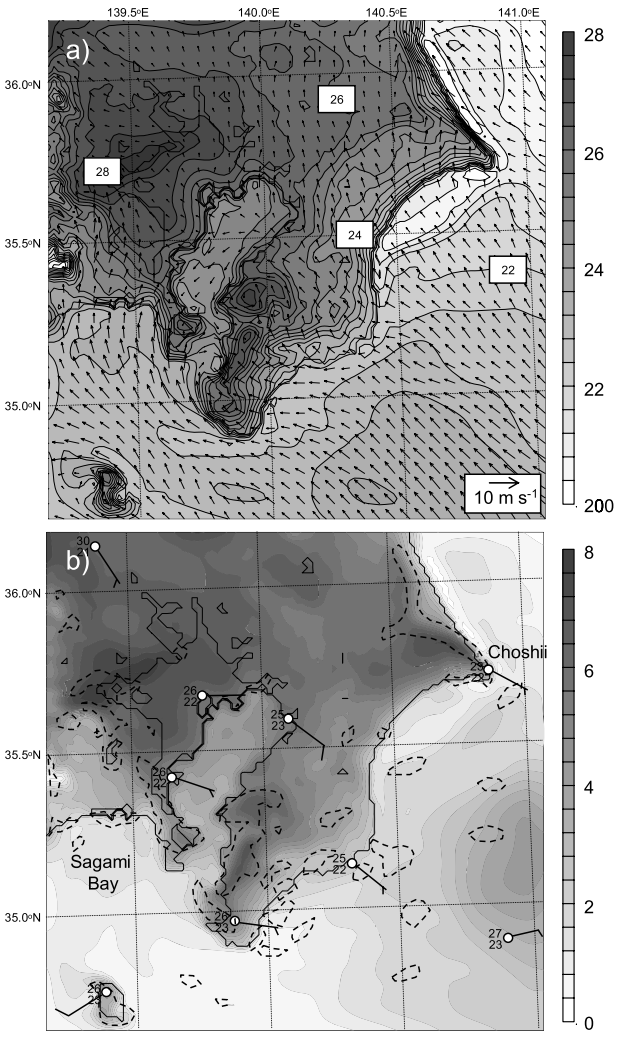

Fig. 10. COAMPS grid 4 (1.67-km) 6-h forecast valid 06 UTC 30 June similar to Fig. 9 but for member 004.

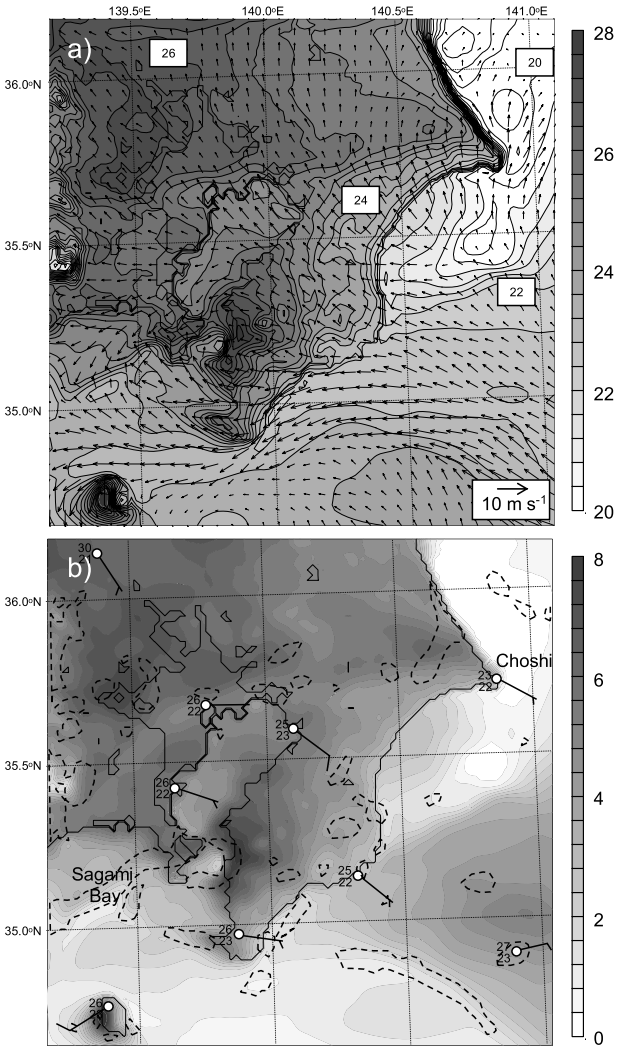

Fig. 11. COAMPS grid 4 (1.67 km) 6-h forecast valid 06 UTC 30 June similar to Fig. 9 but for member 020.

where the largest variations in SST occur (see Fig. 2c). The 6-h forecast valid 06 UTC 30 June for member 020 (Fig. 11) shows that the location of the sea breeze fronts for the perturbed SST members can be dramatically different from the control. Over Sagami Bay the warm SST pool results in a displacement of the front 30–40 km to the south with comparable low-level sea breeze convergence (1.6×10^{-3} versus 1.8×10^{-3} s^{-1} for control). Over the cold upwelled water offshore south of Choshi, enhanced low-level thermal gradients (3.4×10^{-4} versus 8.0×10^{-5} K m^{-1} for control) result in a stronger inland acceleration of the cooler, moister low-level flow compared with the control.

5.3. *Transport and dispersion of passive tracer*

More insight about coastal transport pathways and dynamics are gained through the release of passive tracers within COAMPS at each of the eight validation sites as well as an offshore location approximately 30 km southeast of Katsuura (Fig. 1b). The passive tracers are fully embedded in COAMPS as an in-line module of the prediction system, using the model's exact meteorological fields at each time step and at each gridpoint (Liu et al., 2007). The releases are continuous throughout the model 12-h forecast at a height of 10-m agl. The concentration and dosage fields are log-scaled to arbitrary units (0 to 8) based upon the amount of passive tracer released.

The EXP-3 control 6- and 12-h dosage forecasts for the Tokyo and offshore releases valid at 06 UTC and 12 UTC 27 June 2005 (pre-frontal time) are shown in Fig. 12. Because of the uniform southwesterly low-level flow, the offshore control plume is relatively narrow (∼25–30 km) at both 6- and 12-h. The heavy solid line indicates the envelope of all ensemble members and its correspondence with the control indicates little variation

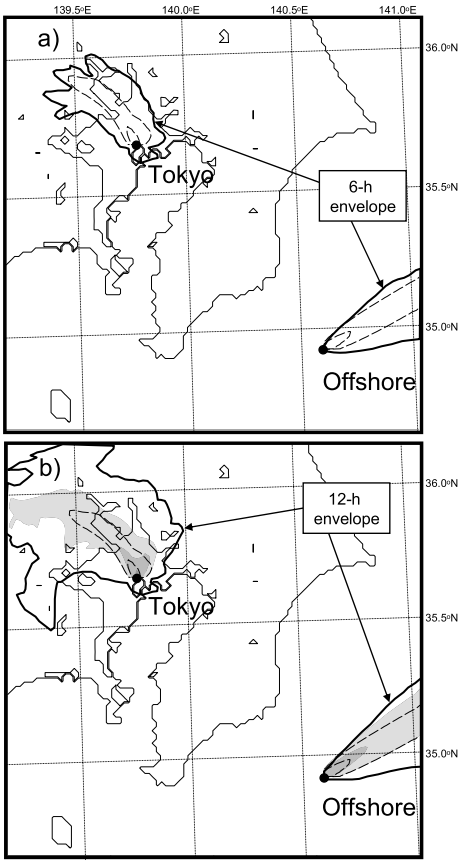

Fig. 12. COAMPS nest 4 passive tracer dosage forecasts (shown for a log threshold value of 2 to 8 units) from 00 UTC 27 June 2005 for release sites Tokyo and Offshore for (a) control 6-h dosage (dashed line) and (b) same as (a) but also showing control 12-h dosage (shaded) with the heavy line indicating the envelope encompassing all perturbation members.

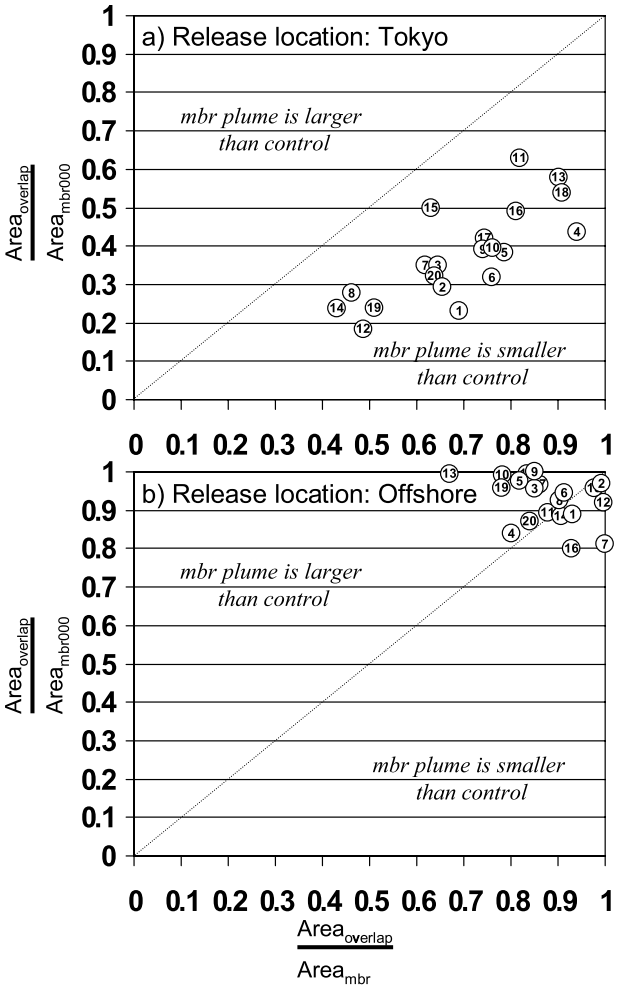

Fig. 13. Measure of effectiveness (MOE) for 12-h forecasts of COAMPS nest-4 (1.67 km) EXP-3 10-m dosage greater than a threshold value (3 units) for a continuous 10-m release of passive tracer valid at 12 UTC 27 June 2005 at (a) Tokyo and (b) Offshore. The number in the data circle is the member number.

among members. There is more variation for the Tokyo release than offshore, with the envelope approximately 30 km wide and 60 km long at 6 h and 50–70 km wide and 80 km long at 12 h. However, the general orientation of the plume for both releases is uni-directional (northeast for the offshore site and northwest for Tokyo), supporting the homogeneous forcing experienced by all members.

The area-based measure of effectiveness (MOE) quantifies the overlap and size of tracer plumes (Warner et al., 2004) and supplies quantitative verification of details gleaned from the tracer dosage (such as Fig. 12) by collapsing plume information from all ensembles onto a single plot. MOE is defined as (Warner et al., 2004)

$$\mathrm{MOE} = (x, y) = \left(\frac{A_{\mathrm{OV}}}{A_{\mathrm{OB}}}, \frac{A_{\mathrm{OV}}}{A_{\mathrm{PR}}}\right) = \left(\frac{A_{\mathrm{OB}} - A_{\mathrm{FN}}}{A_{\mathrm{OB}}}, \frac{A_{\mathrm{PR}} - A_{\mathrm{FP}}}{A_{\mathrm{PR}}}\right) = \left(1 - \frac{A_{\mathrm{FN}}}{A_{\mathrm{OB}}}, 1 - \frac{A_{\mathrm{FP}}}{A_{\mathrm{PR}}}\right) \quad (1)$$

where A_{FN} is the region of false negative, A_{FP} is the region of false positive, A_{OV} is the region of overlap, A_{PR} is the region of the prediction and A_{OB} is the region of the observation. The MOE cannot be used for validation in these experiments because we have no real plume that was measured. Thus, as the purpose of the MOE here is to measure the sensitivity of overlap to changes in initial conditions and or physics parametrizations, A_{OB} is taken as the area of the individual members and A_{PR} is the area of the control member.

Figure 13 shows the MOE of surface dosage for 12-h forecasts valid at 12 UTC 27 June for the Tokyo and offshore releases. For the Tokyo release all members fall below the diagonal, indicating that the size of the dosage footprint of each member is smaller than the control. The slope of the members parallels the diagonal, that is, there is no preference for members with smaller size to

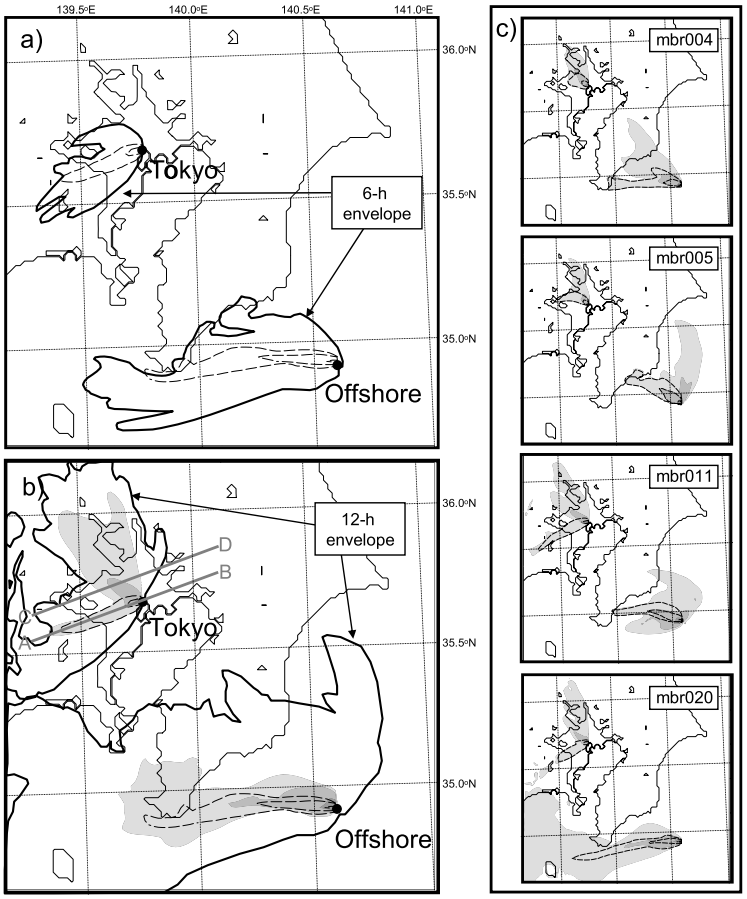

Fig. 14. COAMPS nest 4 passive tracer dosage forecasts (for a log threshold value of 2 to 8 units) for release sites Tokyo and Offshore similar to Figs. 12a and b except valid from 00 UTC 30 June 2005 and (c) 6-h (dashed) and 12-h (shaded) dosage for members 004, 005, 011 and 020.

have larger overlap and vice versa. This further confirms the relatively uniform propagation of the plume as seen in the tracer dosage (Fig. 12b). For the offshore release all members are clustered in the upper right-hand corner, meaning the resultant plumes are all of comparable size and possess a high degree of overlap (Fig. 13b).

The transport and dispersion of the passive tracer for the post-frontal period dominated by the local sea breeze circulation is markedly different. Figure 14 shows the 6- and 12-h control and ensemble envelope dosage valid 06 and 12 UTC 30 June 2005. For Tokyo the 6-h control forecast as well as the ensemble envelope indicate a westward movement of the near-surface plume in response to pre-sea breeze flow from the east (Fig. 14a). The size of the envelope at 6 h is only slightly larger than that for pre-frontal conditions (∼35–40 km wide and 60 km long). The onset of the sea breeze after 06 UTC (15 LT) at Tokyo is evidenced by the shift in the direction of the control and envelope to the north-northwest (Fig. 14b). The width of the ensemble envelope at 12 h is much broader (∼100 to 120 km) than for 27 June (see Fig. 12b).

The passive tracer from the offshore release generally moves to the west by 6 h in all members (Fig. 14a), but shows tremendous spread by 12 h (∼150 km across the entire southern peninsula) as the sea breeze front develops and moves inland. The variability among the individual members (Fig. 14c) illustrates both the bi-directional (west versus north-northwest) nature of the plume footprint at Tokyo due to the sea breeze front and the large spatial extent of the plume westward as well as northward for the offshore release.

Differences in tracer trajectory among the members can be attributed both to the initial ET perturbations and to the urban and SST variations among members. For instance the spread in plumes from the offshore release for members 001 to 009 occurs in a non-urban area, and SST perturbations are not used for those members. Therefore, the differences are due mainly to the perturbations introduced by the ET method. In member 020 cold offshore water (Fig. 2c), in contrast to member 011 (Fig. 2b), leads to a stronger sea breeze flow and accumulation of the tracer over Sagami Bay and against the adjacent coast. So, the linkage of that member's SST variations to the tracer transport and distribution is readily apparent.

The MOE for the 12-h forecasts valid 12 UTC 30 June for the Tokyo and offshore releases reveals the effects of the sea breeze flow (Fig. 15). For the Tokyo release all members fall below the diagonal (as for 27 June) indicating a smaller size plume than the control. For the Offshore release the members fall along the

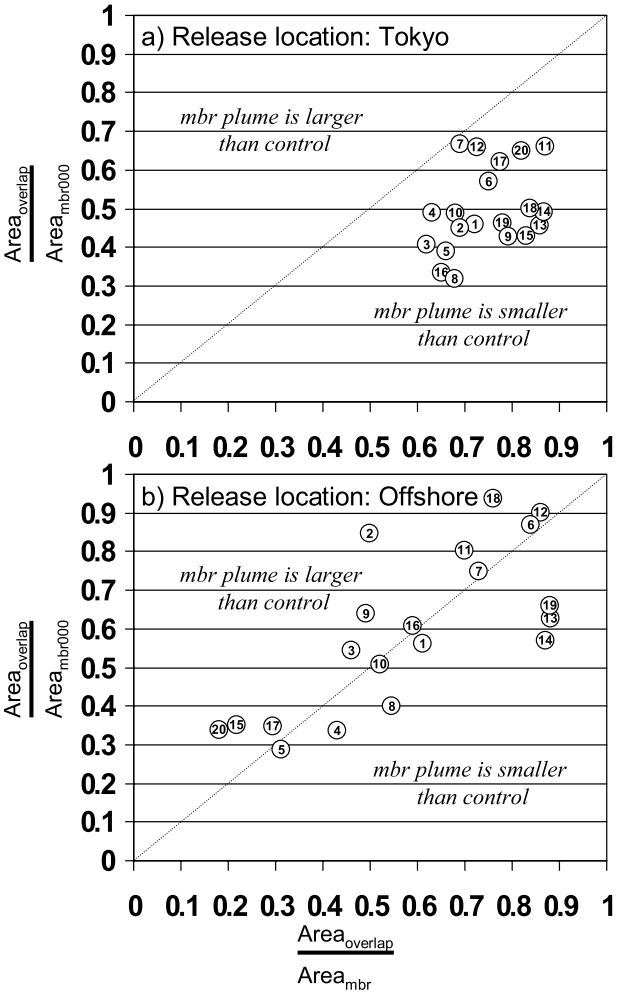

Fig. 15. Measure of effectiveness (MOE) for 12-h forecasts of COAMPS nest-4 (1.67 km) EXP-3 10-m dosage greater than a threshold value (3 units) similar to Fig. 13 except valid at 12 UTC 30 June 2005.

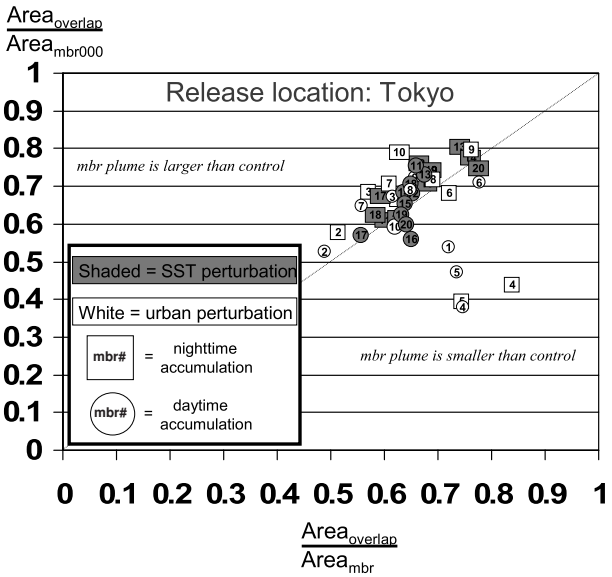

Fig. 16. Measure of effectiveness (MOE) for 12-h forecasts of COAMPS nest-4 (1.67 km) 10-m dosage at Tokyo similar to Fig. 15 but for all 12-h forecasts from 12 UTC 25 June to 00 UTC 1 July. The squares represent accumulation of passive tracer over nighttime (12 UTC to 00 UTC) and circles represent daytime accumulation (00 to 12 UTC).

diagonal, that is, the size of the footprints are approximately the same as the control but vary greatly in overlap. This results in a very large envelope (as shown in Fig. 14b). It is of interest that half of the SST perturbed members are on the extreme ends of the graph. They therefore supply the most variability in terms of degree of overlap with the control during this post-frontal time.

To further explore the sensitivity of the size and overlap of the plume to the structure of member perturbations, Fig. 16 shows the MOE for all 12-h forecasts from 12 UTC 25 June to 1 July 2005 (comprehensive of the whole simulation period). The data are divided into accumulation of passive tracer over approximate nighttime hours (12 to 00 UTC or 21 LT to 09 LT; squares) and daytime (00 to 12 UTC or 09 to 21 LT; circles) as well as perturbations of SST (shaded) or urban (non-shaded). With this larger sample size, it is clear that mbr004 (larger building heights) and mbr005 (larger anthropogenic heating) consistently (both over daytime and nighttime periods) show smaller near-surface plumes and much less overlap (∼0.4) compared with all other members.

The cross-sections shown in Figs. 17 and 18 illustrate the differing dynamic and thermodynamic forcing among members 004 and 005, which contribute to the differences in surface dosage footprints shown in Fig. 14c compared with the control. The cross-sections are aligned approximately parallel to the western shore of Tokyo Bay, transecting the urban area and perpendicular to the mean ensemble sea breeze flow, with the 6-h cross-section (A–B) transecting the Tokyo release site and the primary control dosage footprint and the 12-h cross-section (C–D) approximately 10 km downwind (Fig. 14b). The control 6-h forecast of dosage valid at 06 UTC (15 LT) 30 June shows the cumulative effect of the release over 6 h (from 00 to 06 UTC), whereas the concentration shows the instantaneous plume (at 06 UTC; Fig. 17a). The depth of the dosage plume aligns well with the θ contours and is a good indicator of the depth of the PBL (∼1.2 km at 06 UTC). The dosage is relatively uniform to the left-hand side (west-southwest) of the release ($x = 0$ to 55 km) as the PBL evolves throughout the day and the winds remain fairly steady from the east-northeast. The winds within the PBL indicate a weak low-level jet (~ 4 m s^{-1} at $x = 45$ to 60 km) into the plane of the cross-section (i.e. the leading edge of the sea breeze front as seen in Fig. 9a), with pronounced vertical wind shear above the developing shallow sea breeze (2.3×10^{-2} s^{-1}

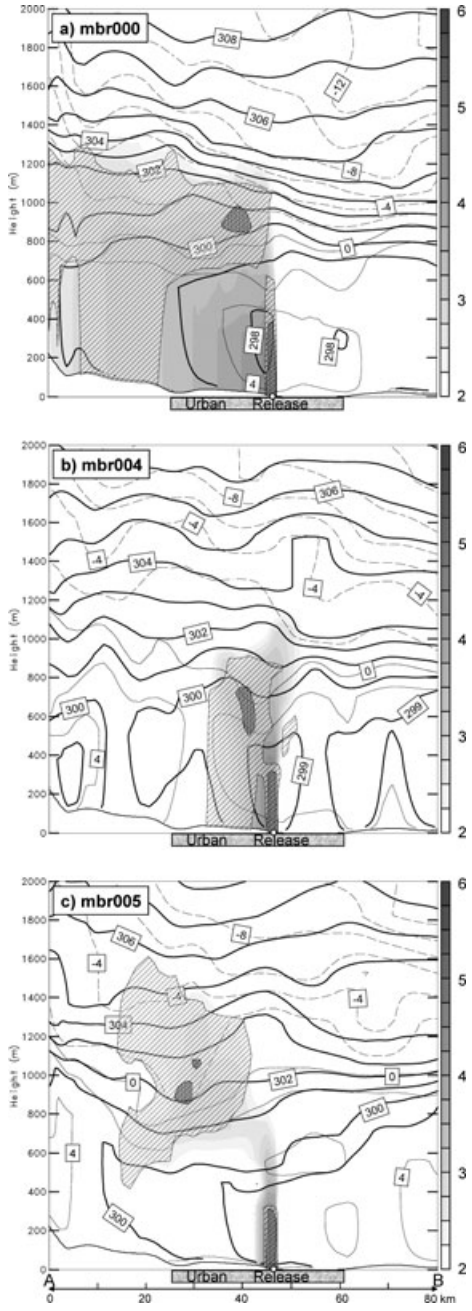

Fig. 17. COAMPS nest-4 vertical cross-section along A–B of Fig. 14 for 6-h forecast valid 06 UTC 30 June 2005 of accumulated dosage (shaded, log units 2 to 6), instantaneous concentration (light hatch = 0, heavy hatch = 1 log units), potential temperature (heavy solid line, interval = 1K) and wind perpendicular to the cross-section (interval = 2 m s^{-1}, thin line; dashed, out of plane) for (a) control member, (b) member 004 and (c) member 005.

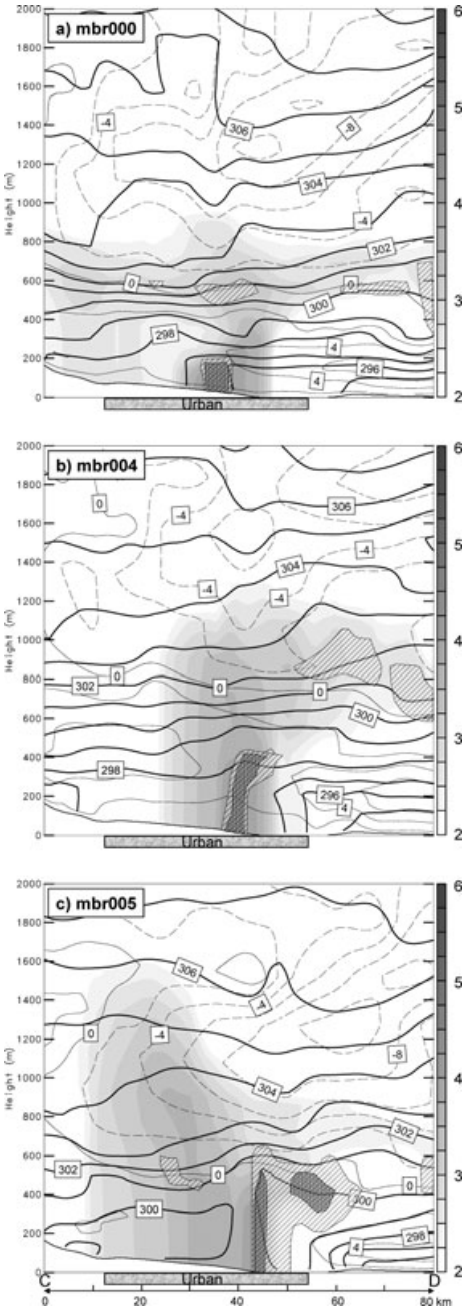

Fig. 18. COAMPS nest-4 vertical cross-section similar to Fig. 17 but along C–D of Fig. 14 for 12-h forecast valid 12 UTC 30 June 2005.

from 0.8 to 1.4 km agl). The instantaneous concentration shows a narrow source plume approximately 400 to 600 m deep with significant mixing of passive tracer to the left-hand side ($x = 0$ to 20 km) reaching the surface.

Compared with the control, 6-h forecasts for members 004 and 005 (Figs. 17b and c) show markedly different structure. There is less lateral dispersion of dosage along the cross-section than is seen in the control. The width of the surface dosage footprint is only 18 km for mbr004 and 5 km for mbr005. This is also evident in the horizontal surface dosage plots (Figs. 14a and c). The plumes for mbr004 and mbr005 are transported more vertically than horizontally, compared with the control. For

member 004 the primary forcing mechanism is mechanically induced turbulence (due to the larger building heights). The maximum PBL TKE for mbr004 along the cross-section over the urban area is 1.6 m^2 s^{-2} (with a vertically-averaged value in the lowest 800 m of 1.0 $m^2 s^{-2}$), compared with a maximum value of 0.8 m^2 s^{-2} (and vertically averaged value of 0.45 m^2 s^{-2}) for the control (figure not shown). The increased mechanical turbulence results in a dosage footprint that is smaller at the surface and confined generally within the urban area (Fig. 17b). Also, the winds are generally weaker than the control, contributing to less lateral spread (see Fig. 10a). For member 005 the dosage plume is vertical up to a depth of ∼800 m with very little lateral spread (see Fig. 14a). This 'chimney' effect is due mainly to increased low-level heating from enhanced anthropogenic heat flux. Along the cross-section over the urban areas, the average sensible heat flux for mbr005 is 225 W m^{-2} compared with 180 W m^{-2} for the control. With the increased surface heating, the capping inversion has reduced magnitude over the urban area for mbr005, resulting in vertical dispersion of concentration up to 1.6 km agl. As in mbr004, the winds are generally weaker for mbr005, lessening the horizontal dispersion.

The 12-h dosage cross-section shows the cumulative daytime heating and turbulence effects (from 09 to 21 LT; Fig. 18). Again, the structure of the three plumes is very different. The control plume is spread laterally, more so than vertically, and the surface dosage extends to regions outside the urban area. Vertically it is confined by a strong capping inversion at ∼0.8 km agl. The surface dosage plumes for mbr004 and mbr005 are confined to the urban areas where the forcing is strongest and do not extend laterally (due to similar forcing mechanisms as discussed in the previous paragraph). Likewise, vertically the extent is much deeper for mbr004 and mbr005. This is reflected in the instantaneous concentrations valid at 12 UTC (21 LT). The control concentration is very shallow (∼180 m) compared with mbr004 (400 m) and mbr005 (600 m), as the daytime PBL begins to erode more quickly for the control (without the enhanced mechanical turbulence or surface heating) and the nighttime residual layer begins to form.

6. Discussion and conclusions

We applied an ensemble approach to generate perturbed members containing different urban and SST representations for the TMA. Initial condition and lateral boundary condition uncertainty in the atmospheric model was accounted for using the ET technique. In the ocean, these uncertainties were approximated using a SST time-lag approach. Uncertainties associated with subgrid scale urban effects were represented by allowing each ensemble member to use differing but reasonable values of primary parameters in two urban canopy models. The ensemble produced several desirable quantitative characteristics. For example, the ensemble representation of initial and boundary condition uncertainty provided by the ET technique led to ensemble forecasts with skillful ensemble mean and a useful spread-skill relationship. The ensemble spread-skill relationship was further improved by the addition of urban perturbations. The ensemble also allowed us to identify parameter settings that either improve or degrade the forecast skill. For urban perturbations, the default values of urban fraction (0.6) and anthropogenic heating (20 W m^{-2}) were found to be too large and too small respectively for Tokyo. For SST perturbations, longer time-lagged SSTs were found to be less skillful.

The ensemble system produced a range of differing sea breeze front behaviours as previously reported in the literature, such as retardation over the urban area (as evidenced by the sea breeze front location spread), enhanced vertical mixing on the periphery of the city (visualized through a tracer released at a downtown Tokyo location) and UHI mitigation. In addition the simulations reflected realistic SST states such as a warm Tokyo Bay and local upwelling southwest of Choshi and in Sagami Bay. These variations in SST steered the sea breeze in subtle ways that had a dramatic impact on tracer distributions emanating from an offshore release.

Passive tracer releases within the ensemble system also indicate (1) that plume dispersion is very sensitive to modelling uncertainties when sea-breeze effects dominate compared with cases in which strong synoptic flow dominates and (2) the lateral extent of surface dosage in urban areas is highly sensitive to building height and urban heating with larger vertical mixing induced by higher building heights and/or larger urban heating leading to smaller surface dosages. Among other things, this second finding suggests that the application of intense low-level heating to toxic releases might help minimize the surface footprint.

Several enhancements to the system are warranted. The representation of urban effects can be refined by incorporating time-varying anthropogenic heating (Sailor and Lu, 2004) and high-resolution building data. Also, more sophisticated SST perturbations will soon be available within the ET framework when multiple ocean model members are simulated, each forced by a distinct atmospheric model member.

Because of its ability to systematically account for key sources of uncertainty due to urban and SST factors, the ensemble framework described and implemented here is poised to become an indispensable tool for meteorological prediction and plume forecasting in complex coastal and urban zones.

7. Acknowledgements

We extend our thanks to Paul May for executing the ocean model simulations. The research was supported by the Navy's Program Executive Office for C4I, Battlespace Awareness and Information Operations Program Office (PMW 120), CAPT Robert Parker under Program Element 0603207N.

References

Barker, E. H. 1992. Design of the navy's multivariate optimum interpolation analysis system. *Wea. Forecast.* **7**, 220–231.

Bishop, C. H. and Toth Z. 1999. Ensemble transformation and adaptive observations. *J. Atmos. Sci.* **56**, 1748–1765.

Bishop, C. H., Holt, T., Nachamkin, J., Chen, S., McLay, J. and Doyle, J. 2008. Regional ensemble forecasts using the Ensemble Transform technique. *Mon. Wea. Rev.*, in press.

Brown, M. J. and Williams, M. 1998. An urban canopy parameterization for mesoscale meteorological models. In: *Proceedings of the Second Symposium on the Urban Environment*. Am. Meteor. Soc., Albuquerque, NM, 144–147.

Chassignet, E. P., Hurlburt, H. E., Smedstad, O. M., Halliwell, G. R., Hogan, P. J. and co-authors. 2007. The HYCOM (hybrid coordinate ocean model) data assimilative system. *J. Mar. Syst.* **65**, 60–83.

Cummings, J. A. 2006. Operational multivariate ocean data assimilation. *Quart. J. Roy. Meteor. Soc.* **131**, 3583–3604.

Dabberdt, W. F. and Miller, E. 2000. Uncertainty, ensembles and air quality dispersion modeling: applications and challenges. *Atmos. Environ.* **34**, 4667–4673.

Delle Monache, L., Deng, X., Zhou, Y. and Stull, R. 2006. Ozone ensemble forecasts, 1: a new ensemble design. *J. Geophys. Res.* **111**, D04304, doi:10.1029/2005JD006310.

Hanna, S. R., Lu, Z. G., Frey, H. C., Wheeler, N., Vukovich, J. and co-authors. 2001. Uncertainties in predicted ozone concentrations due to input uncertainties for the UAM-V photochemical grid model applied to the July 1995 OTAG domain. *Atmos. Environ.* **35**, 891–903.

Harshvardhan, Davies, R., Randall, D. A. and Corsetti, T. G. 1987. A fast radiation parameterization for atmospheric circulation models. *J. Geophys. Res.* **92**, 1009–1016.

Hodur, R. M. 1997. The Naval Research Laboratory's Coupled Ocean/Atmosphere Mesoscale Prediction System (COAMPS). *Mon. Weather Rev.* **125**, 1414–1430.

Holt, T. and Pullen, J. 2007. Urban canopy modeling of the New York City metropolitan area: a comparison and validation of single-layer and multi-layer parameterizations. *Mon. Wea. Rev.* **135**, 1906–1930.

Holt, T. R., Niyogi, D., Chen, F., Manning, K., LeMone, M. A. and co-authors. 2006. Effect of land-atmosphere interactions on the IHOP 24–25 May 2002 convection case. *Mon. Wea. Rev.* **134**, 113–133.

Ichinose, T., Shimodozono, K. and Hanaki, K. 1999. Impact of anthropogenic heat on urban climate in Tokyo. *Atmos. Environ.* **33**, 3897–3909.

Kain, J. S. and Fritsch, J. M. 1993. Convective parameterization for mesoscale models: the Kain- Fritsch scheme. In: *The Representation of Cumulus Convection in Numerical Models*. *Meteorol. Monogr.* Volume 24. Amer. Meteor. Soc., 165–170.

Khairoutdinov, M. and Kogan, Y. 2000. A new cloud physics parameterization in a large eddy simulation model of marine stratocumulus. *Mon. Wea. Rev.* **128**, 229–243.

Klemp, J. B. and Wilhelmson, R. B. 1978. The simulation of three-dimensional convective storm dynamics. *J. Atmos. Sci.* **35**, 1070–1096.

Kusaka, H., Kimura, F., Hirakuchi, H. and Mizutori, M. 2000. The effects of land-use alteration on the sea breeze and daytime heat island in the Tokyo Metropolitan area. *J. Meteorol. Soc. Japan.* **78**, 405–420.

Kusaka, H., Kondo, H., Kikegawa, Y. and Kimura, F. 2001. A simple single-layer urban canopy model for atmospheric models: comparison with multi-layer and slab models. *Bound.-Layer Meteorol.* **101**, 329–358.

Kusaka, H., Chen, F., Tewari, M. and Hirakuchi, H. 2005. Impact of using the urban canopy model on the simulation of the heat island. In: *Proceedings of the WRF/MM5 Users' Workshop*, Boulder, CO, Preprints.

Liu, M., Westphal, D. L., Walker, A. L., Holt, T. R., Richardson, K. A. and co-authors. 2007. COAMPS real-time dust storm forecasting during operation Iraqi freedom. *Wea. Forecast.* **22**, 192–206.

Louis, J.-F., Tiedtke, M. and Geleyn, J. F. 1982. A short history of the operational PBL-parameterization of ECMWF. In: Proceedings of the *Workshop on Planetary Boundary Layer Parameterization*. European Centre for Medium Range Weather Forecasts, Shin-field Park, Reading, Berkshire, UK, 59–79.

Martin, P. J. 2000. A description of the Navy Coastal Ocean Model version 1.0. *Nav. Res. Lab. Rep. NRL/FR/7322–00-9962*, Nav. Res. Lab., Stennis Space Cent., MS, 42 pp.

McLay, J. G., Bishop, C. H. and Reynolds, C. A. 2007. The ensemble-transform scheme adapted for the generation of stochastic forecast perturbations. *Quart. J. Roy. Meteorol. Soc.* **133**, 1257–1266.

Mellor, G. L. and Yamada, T. 1982. Development of a turbulence closure model for geophysical fluid problems. *Rev. Geophys.* **20**, 851–875.

Menut, L. 2003. Adjoint modeling for atmospheric pollution process sensitivity at regional scale. *J. Geophys. Res.* **108**, 8562, doi:10.1029/2002JD002549.

Oda, R., Kanda, M. and Moriwaki, R. 2007. Impact of sea surface temperature on sea air temperature in Tokyo Bay. In: *Proceedings of the Seventh AMS Symposium on the Urban Environment, 10–13 September 2007*, San Diego, CA.

Ohashi, Y. and Kida, H. 2002. Numerical experiments on the weak-wind region formed ahead of the sea-breeze front. *J. Meteorol. Soc.* Japan. **80**, 519–527.

Ooka, R. 2007. Recent development of assessment tools for urban climate and heat-island investigation especially based on experiences in Japan. *Int. J. Climatol.* **27**, 1919–1930.

Pullen, J., Holt, T., Blumberg, A. and Bornstein, R. 2007. Atmospheric response to local upwelling in the vicinity of New York/ New Jersey Harbor. *J. Appl. Meteorol. Climatol.* **46**, 1031–1052.

Rutledge, S. A. and Hobbs, P. V. 1983. The mesoscale and microscale structure and organization of clouds and precipitation in midlatitude cyclones, VIII: a model for the "seeder-feeder" process in warm-frontal rainbands. *J. Atmos. Sci.* **40**, 1185–1206.

Sailor, D. J. and Lu, L. 2004. A top-down methodology for developing diurnal and seasonal anthropogenic heating profiles for urban areas. *Atmos. Environ.* **38**, 2737–2748.

Saitoh, T. S., Shimada, T. and Hoshi, H. 1996. Modeling and simulation of the Tokyo urban heat island. *Atmos. Environ.* **20**, 3431–3442.

Thompson, W., Holt, T. and Pullen, J. 2007. Investigation of a sea breeze front in an urban environment. *Quart. J. Roy. Meteorol. Soc.* **133**, 579–594.

Tran, H., Uchihama, D., Oochi, S. and Yasuoka, Y. 2006. Assessment with satellite data of the urban heat island effects in Asian mega cities. *Int. J. Appl. Earth Observ. Geoinform.* **8**, 34–48.

Warner, T. T., Sheu, R. S., Bowers, J. F., Ian Sykes, R., Dodd, G. C. and co-authors. 2002. Ensemble simulations with coupled atmospheric

dynamic and dispersion models: illustrating uncertainties in dosage simulations. *J. Appl. Meteorol.* **41**, 488–504.

Warner, S., Platt, N. and Heagy, J. F. 2004. User-oriented two-dimensional measure of effectiveness for the evaluation of transport and dispersion models. *J. Appl. Meteorol.* **43**, 53–73.

Yoshikado, H. 1990. Vertical structure of the sea breeze penetrating through a large urban complex. *J. Appl. Meteorol. Climatol.* **29**, 878–891.

Yoshikado, H. and Kondo, H. 1989. Inland penetration of the sea breeze over the suburban area of Tokyo. *Bound.-Layer Meteorol.* **48**, 389–407.

Zhang, F., Bei, N., Nielsen-Gammon, J. W., Li, G., Zhang, R. and co-authors. 2007. Impacts of meteorological uncertainties on ozone pollution predictability estimated through meteorological and photochemical ensemble forecasts. *J. Geophys. Res.* **112**, D04304, doi:10.1029/2006JD007429.